METHODS

A3G preparation and purification

Recombinant, catalytically active A3G was expressed in a baculovirus expression system with an N-terminal glutathione S-transferase (GST) tag[18]. The initial steps in purification were performed essentially as described previously[18]. Briefly, cell lysates treated with DNase I and RNase A were prepared and the soluble fraction was bound to glutathione Sepharose High Performance resin (GE Healthcare) for 3 h at 4 °C. The resin was washed as described[18] and bound GST-A3G was eluted with glutathione buffer (50 mM Tris-HCl, pH 8.0, 1 M NaCl, 40 mM reduced glutathione, 10 μM $ZnCl_2$, 10% glycerol (v/v)). The eluate was filtered through a Acrodisc 25 mm syringe filter with a 1.2 μm Versapor® membrane (Pall Corp.) and was then dialyzed overnight at 4 °C in buffer containing 20 mM Tris-HCl, pH 7.4, 1 M NaCl, 5 mM DTT, and 10% glycerol. Samples were stored at -80 °C prior to further purification. The partially purified GST-A3G was loaded onto a gel filtration column (GE Healthcare, Superdex 200 HiLoad 16/60) pre-equilibrated in a buffer containing 20 mM HEPES, pH 7.4, 200 mM NaCl, 5 mM DTT, and 10% glycerol (v/v). The protein was eluted with the same buffer and the peak corresponding to monomeric GST-A3G was collected and concentrated to an appropriate volume. The GST tag was removed using a Novagen Enterokinase Cleavage Capture Kit. After the cleavage reaction, enterokinase was removed using the capture resin provided in the kit and the GST tag was removed with glutathione Sepharose 4B (GE Healthcare). The deaminase activity of purified A3G was measured using a gel-based uracil DNA glycosylase assay with the 40-nt ssDNA substrate labeled at its 5′ end with Alexa Fluor® 488 (Integrated DNA Technologies, Coralville, IA) instead of ^{32}P[18].

For expression of dimerization-deficient recombinant protein, A3G FW, the pFastBac-GST-A3G FW plasmid was first constructed by cloning an EcoRI–HindIII fragment of pAcG2T-APO3G F126A/W127A (a gift from Myron F. Goodman)[41] into pFastBac1 (Life Technologies) and recombinant virus was obtained using the Bac-to-Bac Baculovirus Expression System (Life Technologies) as previously described[18]. Purification of the A3G FW protein was carried out using our previously reported procedure[18], with the exception of a GST tag-cleaving step and a final purification step. Briefly, Sf21 cells expressing GST-A3G FW were lysed in lysis buffer (25 mM HEPES, pH 7.0, 500 mM NaCl, 1% Triton, 10 mM $CaCl_2$, 1 mM EDTA, 5 mM 2-mercaptoethanol (2-ME), 10% glycerol (v/v), 1 mM PMSF, complete protease inhibitor (Roche Applied Sciences)) and treated with DNase I (5 U/ml, Sigma-Aldrich) and RNase A (40 μg/ml, Qiagen). Cleared cell lysates were then incubated with Glutathione Sepharose 4 Fast Flow resin (GE Healthcare Life Sciences) and subjected to a series of salt washes (500-1000 mM NaCl). The bound GST-A3G FW protein was eluted with the glutathione buffer and the eluate was dialyzed against thrombin cleavage buffer (110 mM Tris HCl, pH 7.4, 100 mM NaCl, 2 mM $CaCl_2$, 1 mM 2-ME, 0.5% TritonX-100). To obtain A3G FW without a GST tag, the dialyzed solution was incubated in the presence of recombinant Thrombin (10 U/ml) (GE Healthcare Life Technologies) at 20 °C for 16 h. The resultant A3G FW was subjected to fractionation with ion exchange chromatography using an SP Sepharose FF Column (GE Healthcare Life Technologies) and collected. The deaminase activity of purified A3G FW was determined without removing the GST tag and was measured using a gel-based uracil DNA glycosylase assay with the 40-nt ssDNA substrate labeled at its 5′ end with FAM (Carboxyfluorescein, Operon Biotechnologies, Japan).

The concentrations of the final monomeric A3G and A3G FW were determined by UV absorbance (ε_{280} = 105,260 $M^{-1}cm^{-1}$) and Bradford assays. The purified proteins were stored at -80 °C.

Single molecule experiments

Single molecule DNA stretching experiments were conducted with dual beam optical tweezers as previously described[40]. Biotin-labeled bacteriophage λ DNA (48.5 kbp, 16.5 μm contour length) was captured between two streptavidin-coated polystyrene beads (Bangs Labs), one fixed on a micropipette

tip and one in the optical trap. The flow chamber was rinsed with buffer (50 mM Na^+, 10 mM HEPES, pH 7.5), and the captured DNA molecule was then stretched and released to obtain a DNA-only force-extension curve (see Supplementary Fig. 1, panel a, black). End-to-end DNA extension is scaled by the total number of base pairs in the molecule to make force-extension curves independent of DNA length. However, the total time for a stretch-release cycle at a fixed pulling rate does depend on DNA length. Specifically, λ DNA increases approximately 10 μm in length during the force-induced melting transition, so going through the transition takes 100 s at the fixed pulling rate of 100 nm/s. DNA release takes the same amount of time.

The Worm-Like Chain (WLC) model describes dsDNA in terms of length b_{ds} at a given force F:

$$b_{ds}(F) = B_{ds}\left[1 - \frac{1}{2}\left(\frac{k_B T}{P_{ds} F}\right)^{\frac{1}{2}} + \frac{F}{S_{ds}}\right] \quad \text{S1}$$

with persistence length P_{ds}, contour length B_{ds}, and stretch modulus S_{ds}. The freely-jointed chain (FJC) model describes ssDNA in terms of length b_{ss} at a given force F:

$$b_{ss}(F) = B_{ss}\left[\coth\left(\frac{2P_{ss}F}{k_B T}\right) - \frac{1}{2}\frac{k_B T}{P_{ss}F}\right]\left[1 + \frac{F}{S_{ss}}\right] \quad \text{S2}$$

The WLC (green) and FJC (blue) polymer models are shown in Supplementary Fig. 1 with typical parameter values (B_{ds} = 0.34 nm/bp, P_{ds} = 48 nm, and S_{ds} = 1200 pN in Eq. S1, B_{ss} = 0.55 nm/bp, P_{ss} = 0.75 nm, and S_{ss} = 720 pN in Eq. S2). A linear combination of the WLC and FJC models describes the measured length b as a function of the fraction of ssDNA generated upon DNA extension f_{ss}[40]:

$$b(f_{ss}) = b_{ds}(1 - f_{ss}) + b_{ss} f_{ss} \quad \text{S3}$$

After three force-extension cycles of DNA alone, the buffer was replaced with protein dilutions ranging from 1 nM to 200 nM A3G. After the initial stretch-release cycle in the presence of A3G, the DNA molecule was stretched again. Incubation was performed at fixed DNA extension above the melting transition (Fig. 2) before the release curve was obtained. The following stretch-release cycle was a control experiment performed without incubation to ensure that the additional binding effect was no longer observed. A 30 s wait time was introduced between each DNA release and the subsequent stretch to ensure complete dissociation of the A3G component exhibiting fast binding kinetics.

Total A3G-ssDNA binding saturated at 200 nM A3G after incubation for 500 s or longer. The force versus extension curve $F(b_{A3G})$ for A3G-saturated ssDNA was phenomenologically described by a second-order polynomial:

$$F(b_{A3G}) = A b_{A3G}^2 + B b_{A3G} + C \quad \text{S4}$$

or, in terms of extension b versus force F:

$$b_{A3G}(F) = \frac{-B + \sqrt{B^2 - 4A(C - F)}}{2A} \quad \text{S5}$$

The parameters of the fit to this polynomial are A = 1713, B = 1028, C = 155 (Fig. 1). The A3G-saturated ssDNA curve was used to analyze fractional A3G binding. Below the melting force F_m = 61.0 ± 0.5 pN, the force-extension curve in the presence of A3G was fit to a linear combination of the dsDNA curve $b_{ds}(F)$ (Eq. S1) and the A3G-saturated curve $b_{A3G}(F)$ (Eq. S5), shown in Supplementary Fig. 1, panel a:

$$b(F < F_m) = b_{ds}(1 - f_{total}) + b_{A3G} f_{total} \quad \text{S6}$$

where f_{total} is fraction of A3G-bound ssDNA. Fits above the melting transition were to a linear combination of $b_{A3G}(F)$ (Eq. S5) and the ssDNA curve $b_{ss}(F)$ (Eq. S2):

$$b(F > F_m) = b_{A3G} f_{total} + b_{ss}(1 - f_{total}) \quad \text{S7}$$

Measurements at forces above the transition were used to confirm that the results of both independent methods agree within error (Supplementary Fig. 1, panel b). Values above and below the melting transition were averaged (data points with propagated error bars not shown), and fraction bound f_{total} as a function of protein concentration c was fit to a simple DNA binding isotherm:

$$f_{total} = \frac{\frac{c}{K_d}}{1 + \frac{c}{K_d}} \quad \text{S8}$$

where K_d is the equilibrium dissociation constant.

Two-step binding model

The kinetics of A3G-ssDNA binding was described as a two-step process, with an initial fast bimolecular binding step that reaches pre-equilibrium before a slow, unimolecular conversion to a more stable complex (Eq. 1). A complete analytical description of this process[48] yields explicit expressions for the fast, slow, and total fractions of A3G bound as a function of time:

$$f_{fast}(t) = P_{total} P_{fast} (e^{-k_{slow} t} - e^{-k_{fast} t}) \quad \text{S9}$$

$$f_{slow}(t) = P_{total} (1 - e^{-k_{slow} t}) \quad \text{S10}$$

$$f_{total}(t) = P_{total} (1 - P_{fast} e^{-k_{fast} t} - (1 - P_{fast}) e^{-k_{slow} t}) \quad \text{S11}$$

where k_{fast} and k_{slow} are binding rates, and P_{fast} and P_{total} are the equilibrium fractions of fast and total complex bound. P_{fast} is the ratio of the forward rate and the total rate for the first step:

$$P_{fast} = \frac{k_1 c}{k_1 c + k_{-1}} \quad \text{S12}$$

Fits to Eqs. S9-S11 (Figs. 3, panels a and b) yield the four parameters k_{fast}, k_{slow}, P_{fast} and P_{total} (reported in supplementary Table 1), which are used to determine the four elementary reaction rates $k_1 c$, k_{-1}, k_2 and k_{-2}, as well as the two equilibrium binding constants K_1 and K_2, for the first and the second binding steps, respectively.

Fast on and off rates

The fast rate k_{fast} is a sum of the forward and backward elementary reaction rates:

$$k_{fast} = k_1 c + k_{-1} \quad \text{S13}$$

where $k_1 c$ is the on rate and k_{-1} is the off rate for the first step, defined in Eq. 1. The model assumes the fast process is bimolecular, so the on rate is proportional to A3G concentration c with rate constant k_1. The data confirms that $k_{fast}(c)$ is linear (Fig. 3, panel c), with bimolecular rate constant k_1 = 2.0 (± 0.1) x 10^5 $M^{-1}s^{-1}$ and off rate k_{-1} = 1.0 (± 0.1) x 10^{-2} s^{-1} (Supplementary Table 2, method A1).

The fast on and off rates were also calculated as follows:

$$k_1 c = k_{fast} P_{fast} \quad \text{S14}$$

The slope of a linear fit to the calculated on rate versus c (Fig. 3, panel c) is an additional measurement of k_1:

$$k_1 c = k_1 c + b \quad \text{S15}$$

where the measured value of k_1 = 1.4 (± 0.1) x 10^5 $M^{-1}s^{-1}$ (Supplementary Table 2, method A2) is consistent with the value from the first method. As expected, the y-intercept of the fit is nearly zero (b = -8 (± 5) x 10^{-4} s^{-1}). The binding model also defines the off rate k_{-1}:

$$k_{-1} = k_{fast}(1 - P_{fast}) \quad \text{S16}$$

which is expected to be concentration-independent (Fig. 3, panel d). Although the linear fit:

$$k_{-1} = mc + k_{-1} \quad \text{S17}$$

yields a non-zero slope (m = 6.1 (± 0.3) x 10^4 $M^{-1}s^{-1}$), the linear dependence is an order of magnitude smaller than that of $k_{fast}(c)$. This measurement of k_{-1} = 1.1 (± 0.1) x 10^{-2} s^{-1} (Supplementary Table 2, method A2) agrees with the value from the first method within error.

The bimolecular rate constant calculated from Eq. S14 is concentration-independent as expected, with a weighted average of k_1 = 1.2 (± 0.1) x 10^5 $M^{-1}s^{-1}$. The k_1 values from the second and third methods agree within error. The off rates calculated from Eq. S16 are also nearly concentration-independent, and the weighted average of the five concentrations is k_{-1} = 2.0 (± 0.2) x 10^{-2} s^{-1} (Supplementary Table 2, method A3).

Fast equilibrium binding constant

The equilibrium binding constant for the bimolecular reaction step, K_1, is a ratio of the forward and backward rates:

$$K_1 = \frac{k_1 c}{k_{-1}} \quad \text{S18}$$

and was calculated from values of $k_1 c$ and k_{-1} obtained from fits. It may also be calculated from $P_{fast}(c)$:

$$K_1 = P_{fast}(1 - P_{fast}) \quad \text{S19}$$

The fast equilibrium binding constant depends linearly upon A3G concentration, as expected (Fig. S2, panel a), and the slope was used to calculate the equilibrium association constant K_1/c (Supplementary Table 2, method C1). Experimentally determined values of k_1 and k_2 were also used to calculate K_1/c directly from Eq. S18 (Supplementary Table 2, method C2). This was used to obtain the equilibrium dissociation constant K_{d1} for the first step:

$$K_{d1} = \frac{c}{K_1} = \frac{k_{-1}}{k_1} \quad \text{S20}$$

The K_d value obtained from this method (127 ± 6 nM) agrees with the K_d of the total fraction bound at t = 50 s of A3G exposure to ssDNA (125 ± 25 nM) fit to a simple DNA binding isotherm (Supplementary Fig. 1, panel b). This is a reasonable observation, in light of the fact that total A3G binding measured after only 50 s is primarily fast binding, which has equilibrated ($1/k_{fast}$ = 24 ± 1 s) while slow binding has not ($1/k_{slow}$ = 206 ± 20 s).

Slow on and off rates

The slow rate k_{slow} is the sum of the forward rate k_2 and backward rate k_{-2}:

$$k_{slow} = k_2 P_{fast} + k_{-2} \quad \text{S21}$$

where the effective forward rate is the product of the conversion rate k_2 and the equilibrium fraction of the fast bound complex P_{fast}. A fit of $P_{fast}(c)$ to Eq. S12 (Fig. S2, panel b) is a fourth method of measuring the fast on and off rates, k_1 = 1.4 (± 0.1) x 10^5 $M^{-1}s^{-1}$ and k_{-1} = 2.1 (± 0.9) x 10^{-2} s^{-1} (Supplementary Table 2, method A4). These values are fixed in the fit of $k_{slow}(c)$ to Eq. S21, which yields k_2 = 7.0 (± 1.0) x 10^{-3} s^{-1} and k_{-2} = 3.0 (± 2.0) x 10^{-5} s^{-1} (Supplementary Table 2, method B1).

An alternative way to calculate these elementary reaction rates involves the slow equilibrium binding constant K_2:

$$K_2 = \frac{k_2}{k_{-2}} \quad \text{S22}$$

which can also be expressed as:

$$K_2 = \frac{1 + \frac{1}{K_1}}{\frac{1}{P_{total}} - 1} \quad \text{S23}$$

Calculations from Eqs. S22 and S23 yield a weighted average of K_2 = 174 ± 16, as reported in Supplementary Table 2 (method D), suggesting that the second binding step is so highly forward-driven that it is nearly irreversible.

The value of K_2 may be used to calculate the forward rate k_2:

$$k_2 = \frac{k_{slow} K_2}{K_2 P_{fast} + 1} \quad \text{S24}$$

and the backward rate k_{-2}:

$$k_{-2} = \frac{k_{slow}}{K_2 P_{fast} + 1} \quad \text{S25}$$

The weighted average of these values is k_2 = 6.6 (± 0.7) x 10^{-3} s^{-1} and k_{-2} = 2.8 (± 0.5) x 10^{-5} s^{-1} (Supplementary Table 2, method B2), which is consistent with the estimate of these rates based on the fit of k_{slow}, as discussed above. Both on and off rates are independent of protein concentration within error (Figure 3, panel d), consistent with a model in which slow binding is unimolecular. Therefore, k_{slow} increases with A3G concentration as fast binding grows, and then saturates with on rate k_2 at high protein concentrations such as those relevant in the virus.

Effect of the STAT3 inhibitor STX-0119 on the proliferation of cancer stem-like cells derived from recurrent glioblastoma

TADASHI ASHIZAWA[1], HARUO MIYATA[1], AKIRA IIZUKA[1], MASARU KOMIYAMA[1], CHIE OSHITA[1], AKIKO KUME[1], MASAHIRO NOGAMI[1], MIKA YAGOTO[1], ICHIRO ITO[2], TAKUMA OISHI[2], REIKO WATANABE[2], KOICHI MITSUYA[3], KENJI MATSUNO[8,9], TOSHIO FURUYA[4], TADASHI OKAWARA[5], MASAMI OTSUKA[6], NAOHISA OGO[7,8], AKIRA ASAI[8], YOKO NAKASU[3], KEN YAMAGUCHI[1] and YASUTO AKIYAMA[1]

[1]Immunotherapy Division, Shizuoka Cancer Center Research Institute, Divisions of [2]Diagnostic Pathology and [3]Neurosurgery, Shizuoka Cancer Center Hospital, Nagaizumi-cho, Sunto-gun, Shizuoka 411-8777; [4]PharmaDesign, Inc., Chuo-ku, Tokyo 104-0032; [5]Kumamoto Health Science University, Kumamoto 861-5598; [6]Faculty of Medical and Pharmaceutical Sciences, Kumamoto University, Kumamoto 862-0973; [7]Shizuoka Institute of Environment and Hygiene, Aoi-ku, Shizuoka 420-8637; [8]Graduate School of Pharmaceutical Sciences, University of Shizuoka, Suruga-ku, Shizuoka 422-8526, Japan

Received January 15, 2013; Accepted March 8, 2013

DOI: 10.3892/ijo.2013.1916

Abstract. Signal transducer and activator of transcription (STAT) 3, a member of a family of DNA-binding molecules, is a potential target in the treatment of cancer. The highly phosphorylated STAT3 in cancer cells contributes to numerous physiological and oncogenic signaling pathways. Furthermore, a significant association between STAT3 signaling and glioblastoma multiforme stem-like cell (GBM-SC) development and maintenance has been demonstrated in recent studies. Previously, we reported a novel small molecule inhibitor of STAT3 dimerization, STX-0119, as a cancer therapeutic. In the present study, we focused on cancer stem-like cells derived from recurrent GBM patients and investigated the efficacy of STX-0119. Three GBM stem cell lines showed many stem cell markers such as CD133, EGFR, Nanog, Olig2, nestin and Yamanaka factors (c-myc, KLF4, Oct3/4 and SOX2) compared with parental cell lines. These cell lines also formed tumors *in vivo* and had similar histological to surgically resected tumors. STAT3 phosphorylation was activated more in the GBM-SC lines than serum-derived GB cell lines. The growth inhibitory effect of STX-0119 on GBM-SCs was moderate (IC_{50} 15-44 μM) and stronger compared to that of WP1066 in two cell lines. On the other hand, the effect of temozolomide was weak in all the cell lines (IC_{50} 53-226 μM). Notably, STX-0119 demonstrated strong inhibition of the expression of STAT3 target genes (c-myc, survivin, cyclin D1, HIF-1α and VEGF) and stem cell-associated genes (CD44, Nanog, nestin and CD133) as well as the induction of apoptosis in one stem-like cell line. Interestingly, VEGFR2 mRNA was also remarkably inhibited by STX-0119. In a model using transplantable stem-like cell lines *in vivo* GB-SCC010 and 026, STX-0119 inhibited the growth of GBM-SCs at 80 mg/kg. STX-0119, an inhibitor of STAT3, may serve as a novel therapeutic compound against GBM-SCs even in temozolomide-resistant GBM patients and has the potential for GBM-SC-specific therapeutics in combination with temozolomide plus radiation therapy.

Correspondence to: Dr Yasuto Akiyama, Immunotherapy Division, Shizuoka Cancer Center Research Institute, 1007 Shimonagakubo, Nagaizumi-cho, Sunto-gun, Shizuoka 411-8777, Japan
E-mail: y.akiyama@scchr.jp

Present address: [9]Graduate School of Medicine, Dentistry and Pharmaceutical Sciences, Okayama University, 1-1-1 Tsushima-naka, Kita-ku, Okayama 700-8530, Japan

Abbreviations: STAT, signal transducer and activator of transcription; SH, Src homology; DMSO, dimethyl sulfoxide; JAK, Janus kinase; T/C, tumor/control; siRNA, small interfering RNA; shRNA, small hairpin RNA

Key words: STAT3, dimerization, phosphorylated STAT3, recurrent glioblastoma, cancer stem cell

Introduction

Glioblastoma multiforme (GBM) is one of the most malignant and aggressive tumors and has a very poor prognosis with a mean survival time of <2 years even with the recent development of temozolomide-based intensive treatment (1,2). Therefore, a new therapeutic approach is urgently needed to control recurrence and overcome resistance to treatment in glioblastoma patients.

GBMs are composed of many types of cells expressing astrocytic and neuronal lineage markers and generated from multipotent stem cells. Recently, GBM stem-like cells (SC) were successfully isolated from human resected tumors using serum-free medium containing epidermal growth factor (EGF) and basic fibroblast growth factor (bFGF) (3-5).

These cells share the properties of normal stem cells like self-renewal and multi-lineage differentiation. The definition according to some research groups is: i) the capability for self-renewal; ii) multi-lineage differentiation; and iii) the ability to regenerate GMB tumors histologically similar to the original tumors in xenografts (6,7). Based on these observations, it is worth attempting to develop therapeutic agents for GMB-SC that affect cell proliferation and resistance to chemo-radiation.

The activation of several signaling pathways including receptor tyrosine kinase (8), Akt (9), MAPK (10), Wnt (11) and Notch and Hedgehog (12) pathways, is involved in the progression of GBM. Importantly, constitutive activation of the Janus kinase (JAK)/signal transducer and activator of transcription (STAT) pathway contributes to the tumor progression by promoting cell proliferation and the inhibition of apoptosis. The STAT protein family is a group of transcription factors that play an important role in relaying signals from growth factors and cytokines (13). STAT3 is reported to be involved in oncogenesis by upregulating the transcription of several genes that control tumor cell survival, resistance to apoptosis, cell cycle progression and angiogenesis. Targets of STAT3 include Bcl-2, Bcl-xL, c-myc, cyclin D1, vascular endothelial growth factor (VEGF) and human telomerase reverse transcriptase.

The association between STAT3 signaling and GBM-SC development has been investigated rigorously (14,15). Sherry *et al* reported that genetic knockdown of stat3 using short hairpin RNA inhibited proliferation and the formation of neurospheres by GBM-SC, indicating that STAT3 can regulate the growth and self-renewal of GBM-SC (14).

Considering STATs are a good target for cancer stem cell therapy, several therapeutic agents including small molecules have been demonstrated to show antitumor effects through the regulation of GBM-SC. Previously, we identified a novel inhibitor of STAT3 dimerization, STX-0119, which exhibited a potent antitumor effect on a human lymphoma cell line with a highly activated STAT3 (16). In the present study, we found that STX-0119 inhibited cell proliferation and the formation of spheres in GBM-SC lines derived from human GBM tumors by regulating STAT3 target genes and inducing apoptosis and suppressed the growth of transplanted tumors of GBM-SC.

Materials and methods

Establishment of primary GB-stem cell lines from GBM patients. GBM tumor samples were obtained from surgically resected materials. The clinical research using tumor tissues from GBM patients was approved by the Institutional Review Board of Shizuoka Cancer Center, Shizuoka, Japan. All patients gave written informed consent.

Tumors were dissociated by teasing with forceps to make a single cell suspension and plated in 25-cm^2 culture flasks in Dulbecco's modified Eagle's medium (DMEM) (Sigma, St. Louis, MO) supplemented with 10% fetal bovine serum (FBS, Invitrogen), penicillin and streptomycin and gentamicin (Invitrogen) for the serum-derived GB cell line. For GBM-SC cultures, dissociated cells were plated in 6-well ultra-low attachment plates (Corning Inc., Corning, NY) in serum-free DMEM supplemented with EGF (Invitrogen) at 20 ng/ml, bFGF (Peprotech, Rocky Hill, NJ) at 20 ng/ml, leukemia inhibitory factor (LIF, Alomone Labs Ltd., Jerusalem, Israel) at 10 ng/ml and B27 (Invitrogen), referred to herein as the stem cell medium (SCM). The cultures were passaged weekly after neurospheres formed.

U87 glioblastoma cell line was purchased from American Type Culture Collection (ATCC, Manassas, VA) and maintained in DMEM containing 10% FBS. The U87 stem cells were cultured like the GBM-SC lines and after 20 passages in SCM were used for experiments *in vitro*.

Among the GBM-SC lines, GB-SCC026 was used for quantitative PCR and apoptosis assay after a 24-h exposure to STX-0119, while GB-SCC010 and 026 cells were utilized in animal experiments.

Antibodies and reagents. Antibodies against STAT3, phospho-specific STAT3 (Tyr705), cleaved caspase-3 and β-actin were purchased from Cell Signaling Technology, Inc. (Danvers, MA) and Becton-Dickinson (BD) Biosciences (Franklin Lakes, NJ) for western blotting (WB). PE-labeled anti-CD133 antibody and FITC-labeled anti-CD44 antibody were purchased from BD Biosciences and used for flow cytometry.

Chemicals. STX-0119 and the JAK-specific inhibitor WP1066 were supplied by The Center for Drug Discovery, University of Shizuoka (Shizuoka, Japan). These compounds were suspended and diluted in a sterile 0.5% w/v methyl cellulose 400-cp solution (Wako, Tokyo, Japan) or dissolved in a mixture of 20% dimethyl sulfoxide (DMSO) (Wako) and 80% polyethylene glycol 300 (Wako) for use in animal experiments.

Flow cytometry. The primary GBM-SC lines or U87 stem cells were stained with the PE-labeled anti-CD133 antibody and FITC-labeled anti-CD44 antibody or isotype control antibodies at a concentration of 10 μg/ml. Stained cells were fixed with 0.5% paraformaldehyde (Sigma-Aldrich) and analyzed on a flow cytometer (FACSCalibur, BD).

Cell proliferation assay. Cell proliferation was examined using the WST-1 assay (Dojin Kagaku Corp., Japan) described previously (16). Briefly, $5x10^3$-$1x10^4$ GBM-SC or U87 stem cells were seeded into each well of a 96-well micro-culture plate (Corning, NY) and compounds diluted with SCM (100-0.25 μM) were added. After 4 days, the WST-1 substrate was added to the culture and optical density (OD) was measured at 450 and 620 nm using an immunoreader (Immuno Mini NJ-2300, Nalge Nunc International, Roskilde, Denmark). The IC_{50} value was defined as the dose needed for a 50% reduction in OD calculated from the survival curve. Percent survival was calculated as follows: (mean OD of test wells - mean OD of background wells) / (mean OD of control wells - mean OD of background wells).

Sphere formation assay. GBM-SC were seeded in a 96-well micro-culture plate at 500 per well and compounds diluted with SCM (100-0.25 μM) were added. After a 7-day incubation at 37°C in a humidified 5% CO_2 atmosphere, the number of spheres with a diameter of >50 μm was counted under a microscope.

Quantitative polymerase chain reaction (qPCR) analysis. The real-time PCR analysis of stem cell and neuronal markers and STAT3 target genes using the 7500 Real-Time PCR system (Applied Biosystems, Foster, CA) was performed as described previously. Briefly, all PCR primers (ABCB1, ALDH1A1, CD44, EGFR, ESA, GFAP, KLF4, NANOG, NES, OLIG2, Oct3/4, CD133, SOX2, TGFBR2, TUBB3, VIM for GB-SC markers; BCL2, Bcl-Xl, Survivin, Cyclin D1, c-Myc, CXCL10, VEGFR2, MMP9, TGFB1, P53, VEGFA, VEGFC, HIF-1α for STAT3 target genes) and TaqMan probes were purchased from Applied Biosystems. GB-stem cell lines or U87 stem cells were treated with STX-0119, WP1066 or DMSO for 24 h and total RNA was extracted. Complementary DNA was synthesized from 100 ng of the total RNA and quantitative PCR was carried using a TaqMan RNA-to-Ct 1-Step kit (Applied Biosystems).

ELISA for human VEGF. VEGF levels in the supernatant of GBM-SC lines and U87 stem cells treated with STX-0119 were measured using human VEGF-specific ELISA. Cells were plated in 96-well ultralow cluster plates (Corning Inc., Corning, NY) in SCM. After 1-day incubation, cells were treated with STX-0119, WP1066 or DMSO for 24 h. Finally, supernatants were collected and VEGF levels were measured.

Western blotting (WB). GBM-SC or U87 stem cells were treated with STX-0119, WP1066 or DMSO at various doses for 24-72 h in SCM. Cells were lysed using RIPA buffer (Thermo Fisher Scientific Inc., Rockford, IL) containing protease inhibitors and phosphatase inhibitors and used for western blotting as described previously. Briefly, cell lysate was subjected to SDS-PAGE with a 7.5% polyacrylamide separating gel and then transferred to PVDF membranes. After blocking, the membranes were incubated at 4°C overnight with the primary antibody against STAT3, phosphospecific STAT3, cleaved caspase-3 and β-actin (1:200-1:2,000) in blocking solution. After a wash, the membranes were incubated for 1 h with horseradish peroxidase (HRP)-conjugated anti-mouse IgG (1:5,000). Membranes were treated with ECL plus reagent (GE Healthcare) and analyzed on a chemiluminescence scanner (LAS-3000, Fujifilm, Tokyo, Japan).

Animal experiments. Immunodeficient male NOD/Shi-*Parkdc*^{scid} (NOD-*scid*) and NOD/Shi-*scid* IL-2Rγ^{null} (NOG) mice (5-6 weeks old) obtained from Nippon Clea (Tokyo, Japan) were used. They were housed in a separate experimental room and given sterilized food and water *ad libitum*. All animals were cared for and used humanely according to guidelines for the welfare and use of animals in cancer research, and procedures approved by the Animal Care and Use Committee of Shizuoka Cancer Center Research Institute.

The GBM-SC lines were re-suspended in RPMI-1640 medium (100 μl) containing Matrigel (BD Biosciences) at 1x10^6/ml and inoculated into the flank of NOD-*scid* and NOG mice. To evaluate the activity against the subcutaneous (s.c.) inoculated tumor cells, tumor volume was calculated based on The National Cancer Institute formula as follows: tumor volume (mm^3) = length (mm) x [width (mm)]^2 x 1/2.

Table I. Frequency of stem cell markers in GB-SC lines.

	CD44$^+$ (%)	CD133$^+$ (%)	CD44$^+$/133$^+$ (%)
GB-SCC010	48.3	10.6	10.4
GB-SCC026	94.6	39.2	37.5
GB-SCC028	82.8	34.4	33.7
U87 stem cell	93.8	72.4	71.6

Immunohistochemistry. Three tumors generated *in vivo* from GBM-SC lines were resected and fixed with formalin solution. Hematoxylin-eosin staining was performed according to the manufacturer's instructions. A pathologist compared the GBM-SC-derived tumor specimen to the surgically resected tumor and made a diagnosis regarding the similarity of the tumors.

Statistical analysis. The statistical analysis was performed with corrected p-values to compare with the untreated control using the Steel multiple plus Kruskal-Wallis method and Mann-Whitney's rank-sum test.

Results

Establishment of primary GBM-SC lines from GBM patients. Three GBM-SC lines (GB-SCC010, 026, 028) were established from 3 GBM patient-derived tumors (Fig. 1A). Each cell line showed a neurosphere feature in SCM. On the other hand, the matched traditionally grown cell line from serum-contained cultures showed an adherent phenotype. Histological analysis of *in vivo* tumors generated from GBM-SC lines demonstrated similar findings to surgically resected tumors (Fig. 1B). All of the GBM-SC lines were shown to be positive for CD133 stain using flow cytometry analysis (Table I).

STAT3 phosphorylation assay. The activation (phosphorylation) of STAT3 was investigated in GBM-SC lines and matched serum-cultured cell lines derived from three GBM patients. Constitutive STAT3 phosphorylation was identified, but was stronger in the GBM-SC lines than serum-cultured cell lines (Fig. 1C).

Expression of stem cell markers in primary GB-SC lines. Quantitative PCR revealed stem cell-related marker gene expression in a representative GBM-SC line, GB-SCC010 (Table II), which showed changes in gene expression compared with the matched primary serum-cultured cell line. The gene expression of stem cell-related markers CD133, EGFR, MDR1, KLF4, Nanog, Nestin, Oct3/4, Olig2, Sox2, VEGFA and vimentin was upregulated >10-fold compared to the serum-cultured cell line. Impressively, the increase of MDR1 gene expression was extraordinarily high, ~200,000-fold. The stem cell-related marker gene expression in the other 2 GBM-SC lines is shown in Table II. Taking the data from all three GBM-SC lines into consideration, CD133, MDR1, Olig2, Sox2 and VEGFA were remarkably upregulated, while TGFBR2 and VEGFR2 were downregulated.

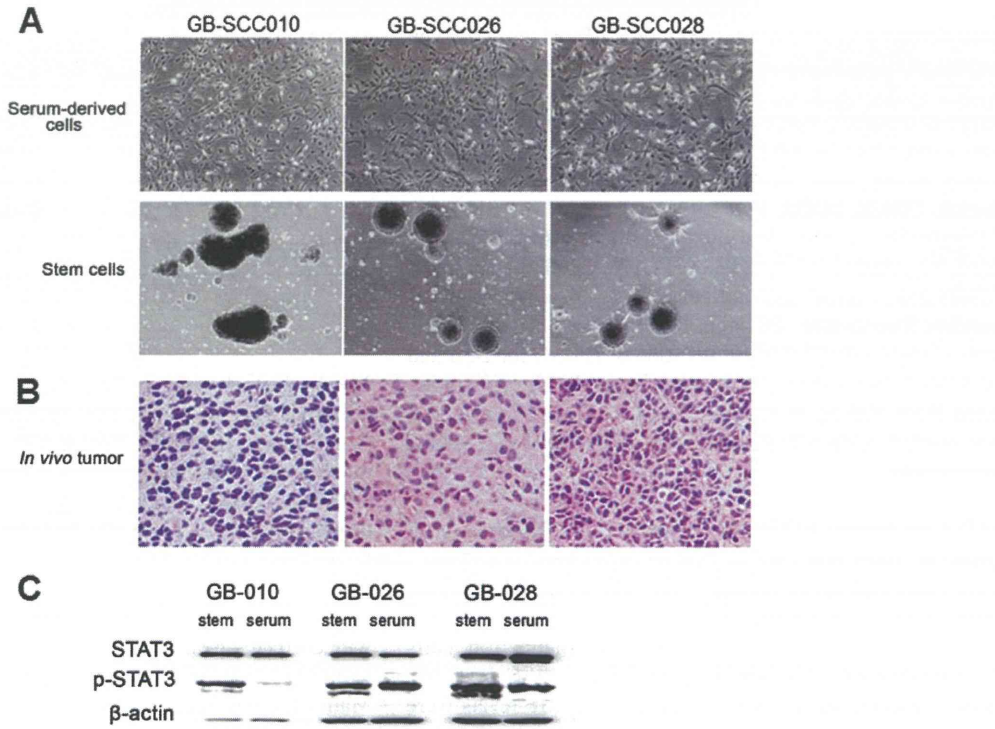

Figure 1. Morphological features and STAT3 phosphorylation of GBM-SC lines. Images of (A) matched serum-derived GBM cell lines (top) and GBM-SC lines (bottom); and (B) tumors generated from GBM-SC lines *in vivo*. Intracerebral transplanted tumors in GB-SCC010 and subcutaneous tumors in other cases (GB-SCC026 and 028 SC lines). Magnification, x100. (C) STAT3 phosphorylation in GBM-SC and matched serum-derived cell lines.

Table II. Frequency of stem cell-associated markers in GB-SC lines.

Gene	GB-010	GB-026	GB-028
ALDH1A1	ND	0.01	5.59
CD133	14.1	27985	3831
CD44	4.68	0.84	45.3
c-Myc	1.92	5.59	0.23
EGFR	48.7	0.17	25.3
ESA	11.7	0.51	49.8
GFAP	4.04	86.5	420
KLF4	27.4	1.21	4.88
MDR1	197220	18.8	783
NANOG	88.3	2.53	448
Nestin	44.7	2.65	398
Oct4/5	69.6	4.87	41.3
OLIG2	124	2035	56420
SOX2	74.3	4635	693
TGFBR2	0.03	0.02	0.06
TUBB3	20.1	17.9	139
VEGFA	77.2	89.1	329
VEGFR2	0.58	0.03	5.76
Vimentin	47.1	3.83	16.8

The quantitative PCR for GBM-stem cell markers was performed using TaqMan probes and specific primers. The expression level in serum-derived cells was rated 1 as a control and gene expression in stem cell lines was shown as fold increase to a control. ND, not detected.

Cell proliferation assay. The growth inhibitory effect of STX-0119 on the GBM-SC lines was moderate (IC_{50} 15-44 μM) and stronger than that of WP1066 in two cell lines (Fig. 2 and Table III). STX-0119 exhibited a stronger inhibitory effect on GB-SCC026 stem cells than the others. On the other hand, the effect of temozolomide was weak in all cell lines (IC_{50} 53-226 μM). The inhibitory effect on U87 stem cell growth did not differ between STX-0119 and WP1066. Additionally, STX-0119 inhibited sphere formation at an IC_{50} of <5 μM and had greater inhibitory activity than WP1066.

Effect of STX-0119 on STAT3 target gene expression and STAT3 phosphorylation. The effect of STX-0119 on STAT3 target gene expression in a representative cell line, GB-SCC026, was analyzed using real-time PCR. STX-0119 significantly inhibited c-myc gene expression in a dose-dependent manner (Fig. 3A). In contrast, WP1066 did not downregulate c-myc expression. C-myc expression in the other GBM-SC lines was not effected by STX-0119 (data not shown). The expression of other STAT3 targets such as Bcl-xL, survivin, cyclin D1, MMP9, TGF-β1, VEGF was also suppressed by STX-0119 at 100 μM (Fig. 3B). Interestingly, the expression of VFGFR2 was remarkably inhibited by STX-0119. STAT3 phosphorylation was moderately down-regulated at 100 μM of STX-0119 in the GB-SCC026 cell line (data not shown). Furthermore, STX-0119 significantly inhibited the stem cell-associated gene expression of CD44, Nanog, nestin and CD133 (Fig. 3C).

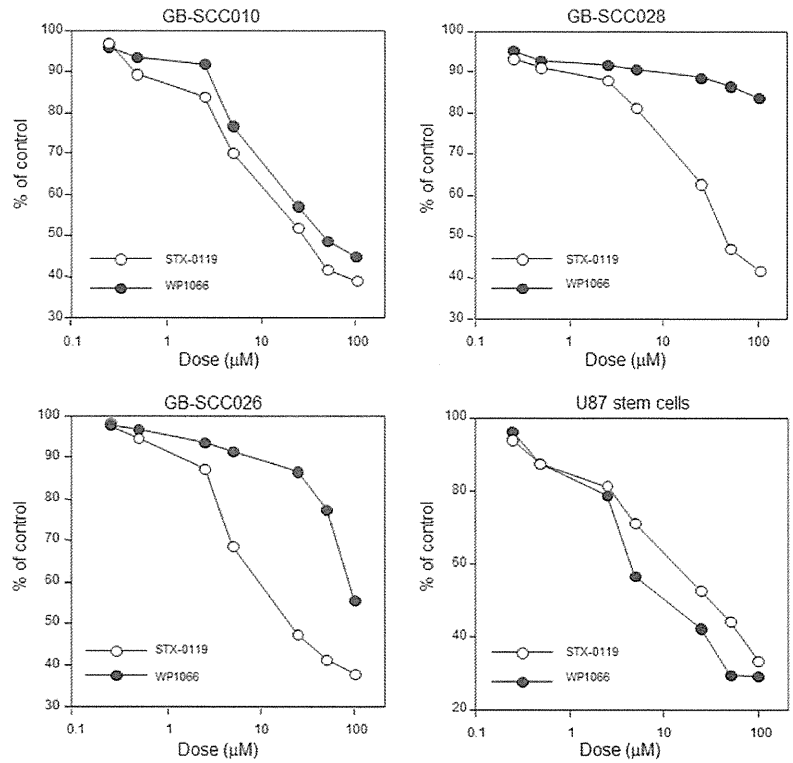

Figure 2. Inhibitory effect of STX-0119 on the proliferation of GBM-SC lines. GBM-SC or U87 stem cells ($5x10^3$-$1x10^4$) were seeded into each well of a 96-well micro-culture plate and various compounds diluted with SCM (100-0.25 μM) were added. Each point shows the mean for three samples. (○) STX-0119; (●) WP1066.

Table III. Effect of STX-0119 and WP1066 on GB-stem cell proliferation.

	Proliferation (IC_{50} /μM)			Sphere (IC_{50} /μM)	
Cell line	TMZ	STX-0119	WP1066	STX-0119	WP1066
GB-SCC010	226	36.1	44.8	3.8	7.8
GB-SCC026	53.1	15.1	>100	4.2	28.9
GB-SCC028	167	44.5	>100	5.2	50.0
U87 parental	45.2	6.6	2.1	-	-
U87 stem cell	66.7	31.4	10.6	2.4	2.2

Induction of apoptosis by STX-0119 in GBM-SC lines. The apoptosis induction in GB-SCC026 cell line and U87 stem cell line was investigated using caspase-3 western detection kit including the primary antibody against cleaved caspase-3 (Cell Signaling). Apoptosis was remarkably identified after a 24-h exposure by STX-0119 with the dose of >50 μM (Fig. 4).

STX-0119 inhibits tumor growth in a subcutaneous model of GBM-SC lines. Based on the growth of transplanted primary GBM-SC lines, GB-SCC010 and 026 were shown to generate well-growing tumors, used as a model of treatment with STX-0119 (Fig. 5A). STX-0119 at doses of 40 and 80 mg/kg suspended with methyl cellulose was orally administered to NOD-*scid* and NOG mice bearing GBM tumors of >35 mm^3. The administration of STX-0119 at 80 mg/kg for three weeks caused a >50% inhibition of GB-SCC010-derived tumors at day 28 (Fig. 5B) and GB-SCC026-derived tumors at day 21, after the start of treatment (Fig. 5C). In contrast, WP1066 did not show an inhibitory effect on GB-SCC026 tumors. Additionally, no significant side effects including weight loss were seen in STX-0119-treated mice. Interestingly, it seemed that the vascularity around the tumor decreased after the STX-0119 administration compared to the GB-SCC026T SC-derived tumor without treatment (Fig. 6A).

Decrease of VEGF production from GBM-SC lines treated with STX-0119. The VEGF levels in the supernatant of GBM-SC

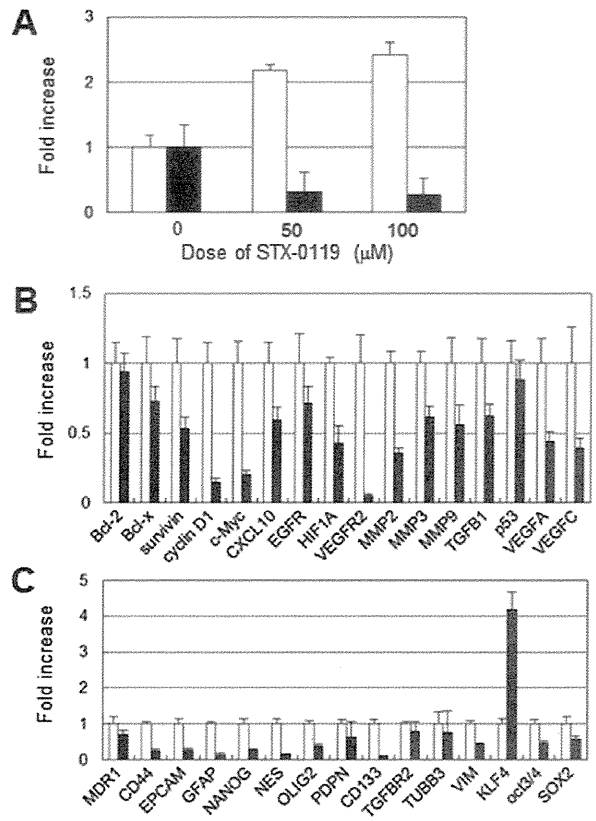

Figure 3. Downregulation of STAT3 target gene expression by STX-0119 in GB-SC lines. The changes in (A) c-myc expression, (B) STAT3 target gene expression and (C) stem cell marker gene expression. (A) GB-SCC026T stem cell line was treated with STX-0119 or WP1066. (B and C) GB-SCC026 stem cell line was treated with 100 μM of STX-0119. The gene expression level without STX-0119 was rated 1 as a control and gene expression in the stem cell line is shown as fold increase. Each column shows the mean ± SD of four determinations. (A) Open column, WP1066; closed column, STX-0119. (B and C) Open column, control; closed column, STX-0119.

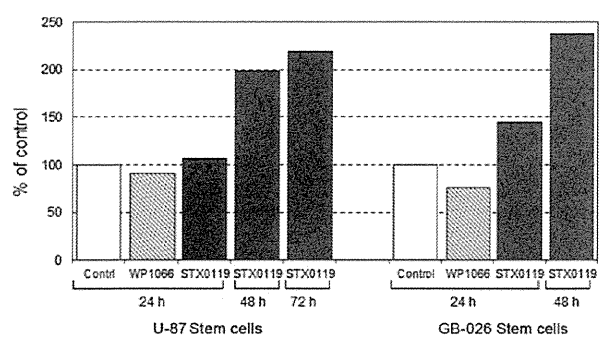

Figure 4. Induction of apoptosis in GBM SC line by STX-0119. Apoptosis was detected using a caspase-3 western detection kit containing a primary antibody against cleaved caspase-3. U87 and GB-SCC026 stem cells were treated with STX-0119 at 100 μM for up to 72 h or WP1066 at 25 μM for 24 h.

lines treated with STX-0119 significantly decreased in a dose-dependent manner (Fig. 6B). Specifically, the reduction was more remarkable in GB-SCC026T SC than 010T SC and U87 cells.

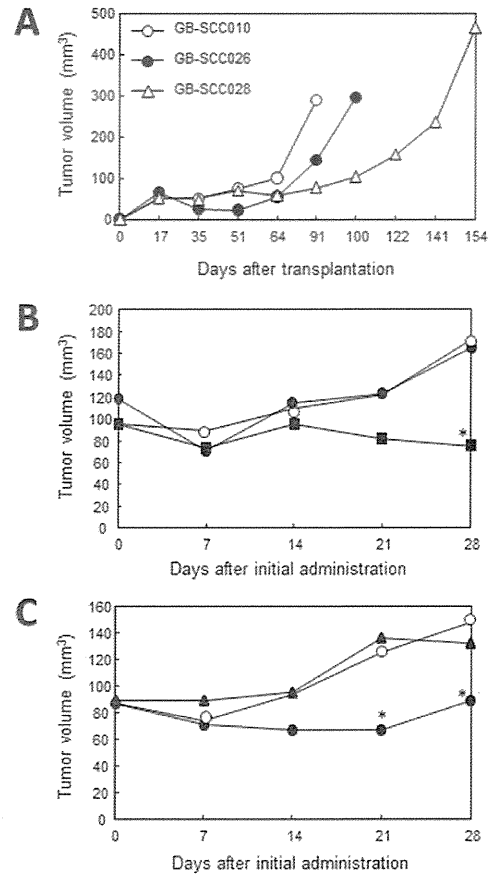

Figure 5. STX-0119 inhibits tumor growth in a subcutaneous model of GB-SC. NOG mice transplanted with human GBM-SC were used. (A) Proliferation of three GBM-SC lines in xenografts. (B) Effect of STX-0119 on GB-010 stem cell growth; (○) control; (●) STX-0119 40 mg/kg; (■) STX-0119 80 mg/kg. (C) Effect of STX-0119 on GB-026 stem cell growth; (○) control; (●) STX-0119 40 mg/kg; (▲) WP1066 40 mg/kg. Each point shows the mean value for 5 mice. *P<0.05, statistically significant compared to control.

Discussion

Glioblastoma multiforme (GBM) is one of the most malignant and aggressive tumors with a very poor prognosis. Despite recent therapeutic advances, less than one-third of GBM patients survive more than 2 years (1,2). Thus, a novel therapeutic approach is urgently needed to control recurrence and overcome resistance to treatment. In the present study, we demonstrated that STX-0119 inhibited GBM-SC proliferation *in vitro* and *in vivo* by downregulating the gene expression of STAT3's targets like BcX-L, cyclin D1, survivin, c-myc, VEGF, MMP2 and HIF-1α and inducing apoptosis. Previously we reported that STX-0119 significantly inhibited the growth of a highly STAT3-phosphorylated lymphoma cell line *in vitro* and *in vivo* by reducing expression c-myc, survivin, cyclin D1 and Bcl-xL and causing apoptosis. The IC_{50} value, 15-44 μM, in the present study regarding GBM-SC lines was higher than that of lymphoma cell line reported previously. Importantly, we demonstrated that higher STX-0119 level than IC_{50} value in mouse blood was obtained *in vivo* in a pharmacokinetic study previously (17).

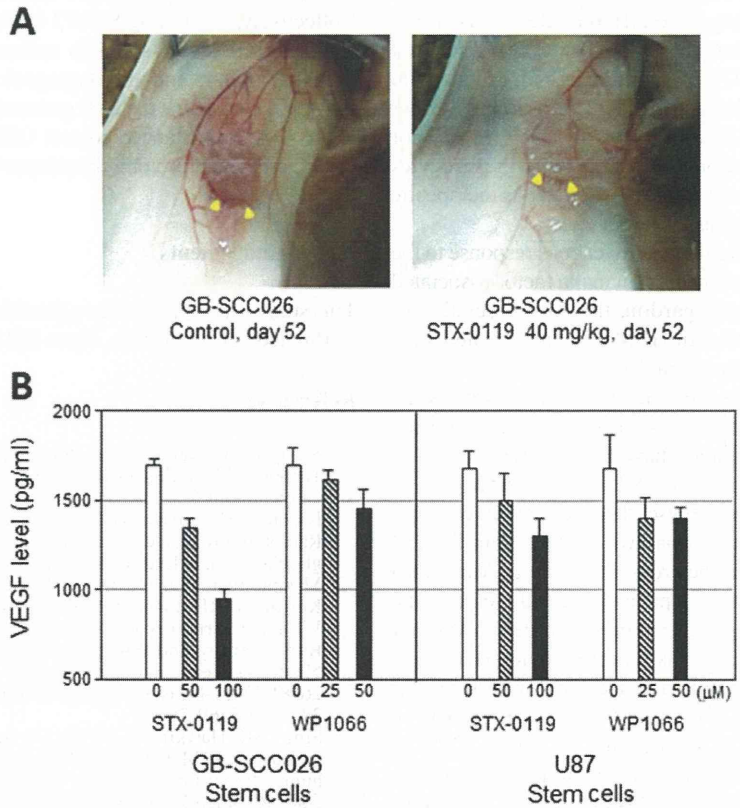

Figure 6. Inhibitory effect of STX-0119 on tumor angiogenesis. (A) The tumor viewed from the reverse side in a GB-SCC026 stem cell-transplanted mouse on day 54. STX-0119 was administered orally daily from day 0 to day 4 followed by 2 days of rest, over a total of 18 days. (B) VEGF levels in the supernatant of U87 and GB-SCC026 stem cells treated with STX-0119 or WP1066 at doses as shown for 48 h. Each column shows the mean of three determinations.

Since GBM-SC were identified as tumor-initiating cells, substantial evidence has been emerged of specific features in terms of gene signatures (6,7,18). The criteria for GBM-SC are as follows: i) isolated and expanded from GBM tumors *in vitro* as neurosphere cultures in serum-free medium containing EGF and bFGF, ii) a capacity for extended self-renewal, multilineage differentiation, iii) the ability to reproduce the histology of human GBM tumors in xenografts and iv) upregulation of drug-resistant and anti-apoptotic genes in response to radiation or chemotherapy. Our three GBM-SC lines met all these criteria. Additionally, we established matched serum-derived cell lines from the same patients. Interestingly, the expression of GBM stem cell markers was weak and the maturation markers GFAP and neuron-specific class III β-tublin were upregulated. Lee *et al* reported that stem cell medium-derived GBM-SC had a specific gene expression signature that more closely resembles the tumor of origin than do serum-derived cell lines from the same tumor (7).

STAT3 is a member of a family of DNA-binding molecules, which regulate numerous physiological and oncogenic signaling pathways leading to target gene expression through STAT3-SH2 dimerization and phosphorylation, promote cell proliferation and induce anti-apoptotic activity, angiogenesis and immunological regulation. Recent studies have showed that STAT3 is constitutively activated in various types of cancers including hematological and solid cancers. Experimental approaches for blocking STAT3 signaling using small interfering RNA (siRNA), small hairpin RNA (shRNA) and STAT3 antisense have been successful in inhibiting cell proliferation *in vitro* (19) and tumor growth *in vivo* (20).

As is the case with GB tumors, the constitutive activation of the STAT3 pathway is linked to tumor promotion and maintenance. With regard to GBM-SC signaling, the interaction between STAT3 and other pathways including EGFR, Notch, Wnt, Hedgehog, Akt, mTOR, olig2, PKC, MAPK, NF-κB and BMP4 was shown to regulate self-renewal (21) and astrocytic differentiation. Interestingly, STAT3 is involved in both stem cell maintenance and astrocytic differentiation, which could be important for therapeutics. Sherry *et al* (14) reported that the stat3 inhibition by shRNA induced growth arrest and inhibition of sphere formation as well as stem cell marker downregulation, which suggested that STAT3 contributes to the maintenance of stem-like characteristics. Our observation in a quantitative PCR assay that one GBM-SC line showed significant inhibition of stem cell markers and STAT3-target genes on STX-0119 treatment, but another GBM-SC line did not, support such a finding. These results might indicate that the dependency on STAT3 differs among GBM-SC lines, perhaps leading to the difference in response to the anti-STAT3 reagent STX-0119. First, it is reasonable to assume

that STX-0119-treated GBM-SC lines become sensitive to apoptotic stimuli when they have differentiated. This would be consistent with the observation that GBM-SC lines do not undergo apoptosis upon STAT3 inhibition in stem cell medium unlike serum-derived glioma cell lines. Additionally, other potential functions of STAT3 in GBM-SC lines, as a tumor suppressor and differentiation-inducing activity in astrocytes (22,23), should be considered to clarify the various therapeutic effects of STX-0119 including off target ones.

A second explanation for the heterogeneous response to the anti-STAT3 agent is activation of Yamanaka factor-associated signaling. Our observation regarding the downregulation of Yamanaka factor expression in GBM-SC lines treated with STX-0119 revealed an unexpected upregulation of KLF-4. The Oct-4 and Sox2 genes were demonstrated to be associated with the maintenance of stemness in glioma-initiating cells (24) and Oct-4 and nanog have been linked to STAT3 signaling (25). Considering that KLF-4 is located downstream of STAT3 and nanog, these observations indicate that KLF-4 signaling is linked to pathways other than STAT3 and nanog. Investigation of the cross talk between Yamanaka factor signaling and the STAT3 pathway should facilitate the development of agents against cancer stem cells. Another interesting point is that KLF-4 is reported to act as a tumor suppressor gene in colorectal cancer cells in which loss of heterozygosity (LOH) and point mutations in KLF-4 gene were identified (26). This observation suggests that KLF-4 might differ from other Yamanaka factors in terms of genetic function and upregulation of KLF-4 is one of mechanisms for the antitumor effect of STX-0119.

GMB-SC-targeted therapeutics such as small molecules and other reagents have been developed. JAK2/STAT3 inhibitors, AZD1480 (27), WP1193 (28) and LLL12 (29), were demonstrated to have inhibitory effects on GB-SCs *in vitro* and *in vivo* mediated by downregulation of GBM stem cell marker as well as STAT3 target genes and induction of apoptosis in stem cells. Curcumin, a natural compound, was shown to suppress tumor growth *in vivo* by inducing autophagy (30). However, anti-GBM-SC agents have yet to be successfully developed. One major reason for this is the significant heterogeneity (31) and involvement of multi-pathway signaling in stem cell growth (21). Novel biomarkers specific for GBM-SC include protein phosphatase 2A (32), inhibitors of DNA binding proteins 2 and 4 (33), IL-13Rα2 (34), Girdin (35) and HIF-1α. These markers have also been shown to be significant prognostic markers. Hypoxia in the tumor microenvironment is crucial to the maintenance of GBM-SC and HIF-1α may be a good GBM stem cell marker at tumor sites (36,37). Additionally, TGF-β1 signaling (38) and EMT factors (39), closely involved in the growth and maintenance of GBM-SC and tumor progression, might be potential targets for treatment. Of note, HIF-1α and TGF-β1 expression was downregulated in STX-0119-treated GBM-SC lines in our study, suggesting these markers to be STAT3 pathway-linked GBM stem cell markers. Another good prognostic marker regarding tumor recurrence in GBM patients is the absence of a mesenchymal transition gene signature (40).

In the present study, we demonstrated that the STAT3 inhibitor STX-0119 significantly inhibited stem cell proliferation *in vitro* and tumor formation *in vivo* by downregulating the gene expression of STAT3 targets and stem cell markers. Collectively, combining STAT3 inhibitors with other reagents targeting GBM-SC-specific molecules (receptor tyrosine kinase inhibitors and anti-angiogenic agents) besides STAT3, may be the basis for the next generation of GBM treatment. It is the most important to control GBM recurrence after standard therapy and prolong the relapse-free and overall survival of GBM patients.

Acknowledgements

This study was supported by a grant from the National Institute of Biomedical Innovation, Japan (06-2).

References

1. Stupp R, Mason WP, van den Bent MJ, Weller M, Fisher B, Taphoorn MJ, Belanger K, Brandes AA, Marosi C, Bogdahn U, Curschmann J, Janzer RC, Ludwin SK, Gorlia T, Allgeier A, Lacombe D, Cairncross JG, Eisenhauer E and Mirimanoff RO: Radiotherapy plus concomitant and adjuvant temozolomide for glioblastoma. N Engl J Med 352: 987-996, 2005.
2. Mirimanoff RO, Gorlia T, Mason W, Van den Bent MJ, Kortmann RD, Fisherb, Reni M, Brandes AA, Curschmann J, Villa S, Cairncross G, Allgerer A, Lacombe D and Stupp R: Radiotherapy and temozolomide for newly diagnosed glioblastoma: recursive partitioning analysis of the EORTC 26981/22981-NCIC CE3 phase III randomized trial. J Clin Oncol 24: 2563-2569, 2006.
3. Singh SK, Hawkins C, Clarke ID, Squire JA, Bayani J, Hide T, Henkeiman RM, Cusimano MD and Dirks PB: Identification of human tumor initiating cells. Nature 432: 396-401, 2004.
4. Galli R, Binda E, Orfanelli U, Cipelletti B, Gritti A, De Vitis S, Fiocco R, Foroni C, Dimeco F and Vescovi A: Isolation and characterization of tumorigenic, stem-like neural precursors from human glioblastoma. Cancer Res 64: 7011-7021, 2004.
5. Singh SK, Clark ID, Terasaki M, Bonn VE, Hawkins C, Squire J and Dirks PB: Identification of a cancer stem cell in human brain tumors. Cancer Res 63: 5821-5828, 2003.
6. Clark MF, Dick JE, Dirks PB, Eaves CJ, Jamieson CH, Jones DL, Visvader J, Weissman IL and Wahl GM: Cancer stem cells-perspectives on current status and future derections: AACR workshop on cancer stem cells. Cancer Res 66: 9339-9344, 2006.
7. Lee J, Kotliarova S, Kotliarov Y, Li A, Su Q, Donin NM, Pastorino S, Purow BW, Christopher N, Zhang W, Park JK and Fine HA: Tumor stem cells derived from glioblastomas cultures in bFGF and EGF more closely mirror the phenotype and genotype of primary tumors than do serum-cultured cell lines. Cancer Cells 9: 391-403, 2006.
8. Brennan C, Momota H, Hambardzumyan D, Ozawa T, Tandon A, Pedraza A and Holland E: Glioblastoma subclasses can be defined by activity among signal transduction pathways and associated genomic alterations. PLoS One 4: e7752, 2009.
9. Cheng CK, Fan QW and Weiss WA: PI3K signaling in glioma-animal models and therapeutic challenges. Brain Pathol 19: 112-120, 2009.
10. Demuth T, Reavie LB, Rennert JL, Nakada M, Nakada S, Hoelzinger DB, Beaudry CE, Henrichs AN, Anderson EM and Berens ME: MAP-ing glioma invasion: mitogen-activated protein kinase 3 and p38 drive glioma invasion and progression and predict patient survival. Mol Cancer Ther 6: 1212-1222, 2007.
11. Pu P, Zhang Z, Kang C, Jiang R, Jia Z, Wang G and Jiang H: Downregulation of Wnt2 and beta-catenin by siRNA suppresses malignant glioma cell growth. Cancer Gene Ther 16: 351-361, 2009.
12. Purow BW, Haque RM, Noel MW, Su Q, Burdick MJ, Lee J, Sundaresan T, Pastorino S, Park JK, Mikolaenko I, Maric D, Eberhart CG and Fine HA: Expression of Notch-1 and its ligands, Delta-like-1 and Jagged-1, is critical for glioma cell survival and proliferation. Cancer Res 65: 2353-2363, 2005.
13. Zhong Z, Wen L and Darnell JE Jr: Stat3 and Stat4: members of the family of signal transducers and activators of transcription. Proc Natl Acad Sci USA 91: 4806-4810, 1994.

14. Sherry MM, Reeves A, Wu JK and Cochran BH: STAT3 is required for proliferation and maintenance of multipotency in glioblastoma stem cells. Stem Cells 27: 2383-2392, 2009.
15. Li GH, Wei H, Lv SQ, Ji H and Wang DL: Knockdown of STAT3 expression by RNAi suppresses growth and induces apoptosis and differentiation in glioblastoma stem cells. Int J Oncol 37: 103-110, 2010.
16. Ashizawa T, Miyata H, Ishii H, Oshita C, Matsuno K, Masuda Y, Furuya T, Okawara T, Otsuka M, Ogo N, Asai A and Akiyama Y: Antitumor activity of a novel small molecule STAT3 inhibitor against a human lymphoma cell line with high STAT3 activation. Int J Oncol 38: 1245-1252, 2011.
17. Matsuno K, Masuda Y, Uehara Y, Sato H, Muroya A, Takahashi O, Yokotagawa T, Furuya T, Okawara T, Otsuka M, Ogo N, Ashizawa T, Oshita C, Tai S, Ishii H, Akiyama Y and Asai A: Identification of a new series of STAT3 inhibitors by virtual screening. ACS Med Chem Lett 1: 371-375, 2010.
18. Carro MS, Lim WK, Alvarez MJ, Bollo RJ, Zhao X, Snyder EY, Sulman EP, Anne SL, Doetsch F, Colman H, Lasorella A, Aldape K, Califano A and Lavarone A: Transcriptional network for mesenchymal transformation of brain tumors. Nature 463: 318-325, 2010.
19. Gao L, Zhang L, Hu J, Li F, Shao Y, Zhao Y, Kalvakolanu DV, Kopecko DJ, Zhao X and Xu DQ: Down-regulation of signal transducer and activator of transcription 3 expression using vector-based small interfering RNAs suppresses growth of human prostate tumor in vivo. Clin Cancer Res 11: 6333-6341, 2005.
20. Ling X and Arlinghaus RB: Knockdown of STAT3 expression by RNA interference inhibits the induction of breast tumors in immunocompetent mice. Cancer Res 65: 2532-2536, 2005.
21. Ohka F, Natsume A and Wakabayashi T: Current trends in targeted therapies for glioblastoma multiforme. Neurol Res Int 2012: doi:10.1155/2012/878425.
22. Takizawa T, Nakashima K, Namihira M, Ochiai W, Uemura A, Yanagisawa M, Fujita N, Nakao M and Taga T: DNA methylation is a critical cell-intrinsic determinant of astrocyte differentiation in the fetal brain. Dev Cell 1: 749-758, 2001.
23. De la Iglesia N, Konopka G, Puram SV, Chan JA, Bachoo RM, You MJ, Levy DE, Depinho RA and Bonni A: Identification of a PTEN-regulated STAT3 brain tumor suppressor pathway. Genes Dev 22: 449-462, 2008.
24. Ikushima H, Todo T, Ino Y, Takahashi M, Saito N, Miyazaki K and Miyazono K: Glioma-initiating cells retain their tumorigenicity through integration of the Sox axis and Oct4 protein. J Biol Chem 286: 41434-41441, 2011.
25. Guo Y, Mantel C, Hromas RA and Broxmeyer HE: Oct-4 is critical for survival/antiapoptosis of murine embryonic stem cells subjected to stress: effects associated with Stat3/survivin. Stem Cells 26: 30-34, 2008.
26. Zhao W, Hisamuddin IM, Nandan MO, Babbin BA, Lamb NE and Yang VW: Identification of Krüppel-like factor 4 as a potential tumor suppressor gene in colorectal cancer. Oncogene 23: 395-402, 2004.
27. McFarland BC, Ma JY, Langford CP, Gillespie GY, Yu H, Zheng Y, Nozell SE, Huszar D and Benveniste EN: Therapeutic potential of AZD1480 for the treatment of human glioblastoma. Mol Cancer Ther 10: 2384-2393, 2011.
28. Sai K, Wang S, Balasubramaniyan V, Conrad C, Lang FF, Aldape K, Szymanski S, Fokt I, Dasgupta A, Madden T, Guan S and Chen Z: Induction of cell-cycle arrest and apoptosis in glioblastoma stem-like cells by WP1193, a novel small molecule inhibitor of the JAK2/STAT3 pathway. J Neurooncol 107: 487-501, 2012.
29. Ball S, Li C, Li PK and Lin J: The small molecule, LLL12, inhibits STAT3 phosphorylation and induces apoptosis in medulloblastoma and glioblastoma cells. PLoS One 6: e18820, 2011.
30. Zhuang W, Long L, Zheng B, Ji W, Yang N, Zhang Q and Liang Z: Curcumin promotes differentiation of glioma-initiating cells by inducing autophagy. Cancer Sci 103: 684-690, 2012.
31. Denysenko T, Gennero L, Roos MA, Melcarne A, Juenemann C, Faccani G, Morra I, Cavallo G, Reguzzi S, Pescarmona G and Ponzetto A: Glioblastoma cancer stem cells: heterogeneity, microenvironment and related therapeutic strategies. Cell Biochem Funct 28: 343-351, 2010.
32. Hofstetter CP, Burkhardt JK, Shin BJ, Gursel DB, Mubita L, Gorrepati R, Brennan C, Holland EC and Boockvar JA: Protein phosphatase 2A mediates dormancy of glioblastoma multiforme-derived tumor stem-like cells during hypoxia. PLoS One 7: e30059, 2012.
33. Wu Y, Richrad JP, Wang SD, Rath P, Laterra J and Xia S: Regulation of glioblastoma multiforme stem-like cells by inhibitor of DNA binding proteins and oligodendroglial lineage-associated transcription factors. Cancer Sci 103: 1028-1037, 2012.
34. Nguyen V, Conyers JM, Zhu D, Gibo DM, Dorsey JF, Debinski W and Mintz A: IL-13Rα2-targeted therapy escapees: biologic and therapeutic implications. Transl Oncol 4: 390-400, 2011.
35. Natsume A, Kato T, Kinjo S, Enomoto A, Toda H, Shimato S, Ohka F, Motomura K, Kondo Y, Miyata T, Takahashi M and Wakabayashi T: Girdin maintains the stemness of glioblastoma stem cells. Oncogene 31: 2715-2724, 2012.
36. Pistollato F, Abbadi S, Rampazzo E, Persano L, Della Puppa A, Frasson C, Sarto E, Scienza R, D'Avella D and Basso G: Intratumoral hypoxic gradient drives stem cells distribution and MGMT expression in glioblastoma. Stem Cells 28: 851-862, 2010.
37. Qiang L, Wu T, Zhang HW, Lu N, Hu R, Wang YJ, Zhao L, Chen FH, Wang XT, You QD and Guo QL: HIF-1α is critical for hypoxia-mediated maintenance of glioblastoma stem cells by activating Notch signaling pathway. Cell Death Differ 19: 284-294, 2012.
38. Ikushima H, Todo T, Ino Y, Takahashi M, Miyazawa K and Miyazono K: Autocrine TGF-β signaling maintains tumorigenicity of glioma-initiating cells through Sry-related HMG-box factors. Cell Stem Cell 5: 504-514, 2009.
39. Kaur H, Phillips-Mason PJ, Burden-Gulley SM, Kerstetter-Fogle AE, Basilion JP, Sloan AE and Brady-Kalnay SM: Cadherin-11, a marker of the mesenchymal phenotype, regulates glioblastoma cell migration and survival in vivo. Mol Cancer Res 10: 293-304, 2012.
40. Cheng WY, Kandel JJ, Yamshiro DJ, Canoll P and Anastassiou D: A multi-cancer mesenchymal transition gene expression signature is associated with prolonged time to recurrence in glioblastoma. PLoS One 7: e34705, 2012.

OPEN ACCESS Freely available online

PLOS | ONE

APOBEC3G Oligomerization Is Associated with the Inhibition of Both *Alu* and LINE-1 Retrotransposition

Takayoshi Koyama[1☯], Juan Fernando Arias[1☯], Yukie Iwabu[1], Masaru Yokoyama[2], Hideaki Fujita[3], Hironori Sato[2], Kenzo Tokunaga[1*]

1 Department of Pathology, National Institute of Infectious Diseases, Tokyo, Japan, **2** Pathogen Genomics Center, National Institute of Infectious Diseases, Tokyo, Japan, **3** Faculty of Pharmaceutical Sciences, Nagasaki International University, Nagasaki, Japan

Abstract

Alu and LINE-1 (L1), which constitute ~11% and ~17% of the human genome, respectively, are transposable non-LTR retroelements. They transpose not only in germ cells but also in somatic cells, occasionally causing cancer. We have previously demonstrated that antiretroviral restriction factors, human APOBEC3 (hA3) proteins (A–H), differentially inhibit L1 retrotransposition. In this present study, we found that hA3 members also restrict *Alu* retrotransposition at differential levels that correlate with those observed previously for L1 inhibition. Through deletion analyses based on the best-characterized hA3 member human APOBEC3G (hA3G), its N-terminal 30 amino acids were required for its inhibitory activity against *Alu* retrotransposition. The inhibitory effect of hA3G on *Alu* retrotransposition was associated with its oligomerization that was affected by the deletion of its N-terminal 30 amino acids. Through structural modeling, the amino acids 24 to 28 of hA3G were predicted to be located at the interface of the dimer. The mutation of these residues resulted in abrogated hA3G oligomerization, and consistently abolished the inhibitory activity of hA3G against *Alu* retrotransposition. Importantly, the anti-L1 activity of hA3G was also associated with hA3G oligomerization. These results suggest that the inhibitory activities of hA3G against *Alu* and L1 retrotransposition might involve a common mechanism.

Citation: Koyama T, Arias JF, Iwabu Y, Yokoyama M, Fujita H, et al. (2013) APOBEC3G Oligomerization Is Associated with the Inhibition of Both *Alu* and LINE-1 Retrotransposition. PLoS ONE 8(12): e84228. doi:10.1371/journal.pone.0084228

Editor: Chen Liang, Lady Davis Institute for Medical Research, Canada

Received October 23, 2013; **Accepted** November 20, 2013; **Published** December 19, 2013

Funding: This work was supported by grants from the Ministry of Health, Labor and Welfare of Japan (Research on HIV/AIDS project no.H24-005, H24-008 and H25-010), and from the Ministry of Education, Science, Technology, Sports and Culture of Japan (22590428). The funders had no role in study design, data collection and analysis, decision to publish, or preparation of the manuscript.

Competing interests: The authors have declared that no competing interests exist.

* Email: tokunaga@nih.go.jp

☯ These authors contributed equally to this work.

Introduction

Retrotransposons compose ~42% of the human genome, and these elements are classified into the non-LTR and LTR classes. Non-LTR retrotransposons are subdivided into long interspersed elements (LINEs) and short interspersed elements (SINEs), representatives of which are LINE-1 (L1) and *Alu*, which comprise ~17% and ~11% of the human genome, respectively [1]. L1 elements harbor two ORFs: ORF1, which encodes an RNA-binding protein, and ORF2, which encodes an endonuclease-like and reverse transcriptase-like protein. After translation, these proteins bind to the L1 RNA to form a ribonucleoprotein particle that is imported into the nucleus to be integrated into the genome through target-primed reverse transcription [2-4]. Unlike L1, *Alu* elements do not encode a reverse transcriptase or an endonuclease; rather, the transcribed *Alu* RNAs hijack the L1-encoded enzymes to move to new locations in the genome through mechanisms that are as yet unclear [5]. Importantly, retrotransposition by L1 and *Alu* occurs not only in germ cells, causing several genetic diseases [6-13], but also in somatic cells, such as brain tissues [14,15], and malignant tissues and cells such as B-cell lymphoma cells [16], breast carcinoma tissue [17], colon carcinoma tissue [18], and hepatocellular carcinoma tissue [19]. These facts indicate that an intrinsic protection system should function properly to suppress these types of retrotransposition in normal somatic cells.

Human APOBEC3G (hA3G) is one of the seven members of the APOBEC3 (hA3) family of cytidine deaminases (hA3A to hA3H). hA3G is known to be an intrinsic retroviral restriction factor that inhibits Vif-defective human immunodeficiency virus type 1 (HIV-1) infection by being incorporated into viral particles and mediating extensive deamination of the nascent minus-strand viral DNA during reverse transcription, which results in G-to-A hypermutation [20-23]. This antiretroviral restriction extends to not only exogenous retroviruses, such as

simian immunodeficiency virus [24-27], primate foamy virus [28,29], human T-cell leukemia virus type I [30], murine leukemia virus [21,26,31], mouse mammary tumor virus [32], and equine infectious anemia virus [22] , but also endogenous retroelements, such as the MusD and intracisternal A-particle LTR murine retrotransposons and, as described below, human *Alu* and L1 retrotransposons ([33-40]; see also review in ref[41].). hA3G also restricts infection by hepatitis B virus, which replicates its DNA genome by reverse transcription of an RNA intermediate [42,43]. Whereas pre-primate mammals encode one, two to three A3 proteins [44], primates have acquired seven different A3 genes through 33 million years of evolution [45]. Such expansion of the hA3 genes correlates with an abrupt reduction in retrotransposition activity in primates, suggesting that these proteins have evolved to protect hosts from the genomic instability caused by retroelements [46].

We previously reported that hA3 family proteins have differential levels of anti-L1 activity that do not correlate with either antiretroviral activity or subcellular localization patterns [37]. Although several groups that performed similar studies showed that hA3G has little or no anti-L1 activity [47-50], we and others have found that the hA3G is indeed able, albeit less potently than hA3A or hA3B, to restrict L1 retrotransposition [37-40]. Such discrepancies might be attributed to the cell-type-dependent expression levels of hA3G, as we previously demonstrated [37]. We also found that hA3G inhibits L1 retrotransposition independently of its deaminase activity, which is primarily required for its antiretroviral function, and hA3G likely prevents L1 DNA synthesis *per se* [37]. With regard to the inhibition of *Alu* by hA3 family members, several groups have reported that hA3A, hA3B [49], hA3G [34-36], hA3DE, and hA3H [51] inhibit *Alu* retrotransposition. In this study, we found that all hA3 family members, from hA3A to hA3H, are able to inhibit *Alu* retrotransposition. The inhibitory effect of hA3G on *Alu* retrotransposon was associated with the N-terminal 30 amino acid residues and with hA3G's oligomerization activity, but not with its deaminase activity. Structural modeling showed that amino acid positions 24–28 are responsible for the oligomerization of hA3G. This result was verified by immunoprecipitation using an hA3G mutant with amino acid substitutions at these positions. Consistent with this result, we found that amino acid positions 24–28 of hA3G are critical for its inhibitory activity against *Alu* retrotransposon. Importantly, these amino acids were also shown to be important for L1 inhibition, suggesting that both *Alu* and L1 retrotransposition might be restricted by similar mechanisms involving hA3G, which require the oligomerization of this restriction factor.

Materials and Methods

DNA constructs

The hemagglutinin (HA)-tagged hA3 expression plasmids (phA3A-HA, phA3B-HA, phA3C-HA, phA3DE-HA, phA3F-HA, phA3G-HA, and phA3H-HA), the GFP expression plasmid pCA-EGFP, the empty expression vector pCAGGS-HA, the L1 indicator construct pCEP4/L1mneoI/ColE1 (kindly provided by N. Gilbert), the L1 ORF2 expression plasmid pBudORF2opt (kindly provided by A.M. Roy-Engel), the *Alu* indicator construct pYa5neotet (kindly provided by T. Heidmann), Vif-deficient HIV-1 proviral indicator construct pNLLuc-F(-)E(-), and VSV-G expression plasmid pHIT/G have previously been described elsewhere [5,37,52-55] (note that the hA3h expression plasmid encodes the haplotype I). The myc-tagged version of the wild-type hA3G expression plasmid, phA3G-myc, was also created. A series of N-terminal deletion mutants of hA3G (phA3G-NΔ30-HA, -NΔ60-HA, -NΔ90-HA, -NΔ120-HA, and -NΔ150-HA) were created by inserting serially deleted PCR fragments of hA3G into the mammalian expression plasmid pCAGGS with a C-terminal HA-tag. The deaminase-deficient mutant (phA3G-E259Q-HA), the oligomerization-deficient mutant (phA3G-C97/100A-HA), and the N-terminal mutants (phA3G-5G(24–28)-HA, phA3G-4G(124–127)-HA, phA3G-R24G-HA, and phA3G-Y125G-HA) of hA3G were created using phA3G-HA as a template with a QuikChange site-directed mutagenesis kit (Stratagene).

Cell maintenance, transfections, and protein analyses

HeLa and 293T cells were maintained under standard conditions. 293T cells were transfected with HA-tagged hA3 wild-type and mutant plasmids using the FuGENE 6 transfection reagent (Roche Applied Science) according to the manufacturer's instructions. Cell extracts from transfected cells were subjected to gel electrophoresis and then transferred to a nitrocellulose membrane. The membranes were probed with an anti-HA mouse monoclonal antibody (Sigma). The antibody-bound proteins were visualized to confirm hA3 protein expression by chemiluminescence using an ECL Western blotting detection system (GE Healthcare) and an LAS-3000 imaging system (FujiFilm).

Immunofluorescence microscopy

HeLa cells were plated on 13-mm glass coverslips and transfected with 0.5 μg of hA3 expressing plasmids by using FUGENE6. The transfected cells were fixed with 4% paraformaldehyde at room temperature for 30 min, permeabilized with 0.05% saponin for 10 min, and immunostained with an anti-HA monoclonal antibody (5 μg/ml). The secondary goat anti-mouse antibody that was conjugated with Cy3 was used at 5 μg/ml. All immunofluorescence images were observed on a Leica DMRB microscope (Wetzlar, Germany) equipped with a 63×1.32 NA oil immersion lens (PL APO), acquired through a cooled CCD camera, MicroMAX (Princeton Instruments, Trenton, NJ), and digitally processed using IPlab Software (Scanalytics, Fairfax, VA). All images were assembled using Adobe Photoshop (Adobe Systems, Mountain View, CA).

L1 and Alu retrotransposition assay

L1 and *Alu* retrotransposition assays were performed by co-transfecting 2 x 10^5 HeLa cells with 0.1 μg of the respective hA3 expression plasmid (or a mock expression vector, pCAGGS-HA, as a positive control) together with either 0.3 μg of the neomycin-resistance (neo^r)-based L1 expression vector pCEP4/L1mneoI/ColE1 and 0.1 μg of an empty vector (for the

L1 retrotransposition assay) or 0.3 μg of the neo^r-based *Alu* expression vector pYa5neotet and 0.1 μg of the L1 ORF2 expression plasmid pBudORF2opt (for the *Alu* retrotransposition assay) using Lipofectamine and Plus reagents (Invitrogen). As a negative control, 0.5 μg of a GFP expression vector, pCA-EGFP, was transfected into HeLa cells. After 72 h, the cells were trypsinized, re-seeded into T25 or T75 flasks for G418 selection (1 mg/ml for the L1 assay and 400 μg/ml for the *Alu* assay), and maintained. At 14 days after selection, the resultant G418-resistant (G418^R) colonies were fixed, stained with crystal violet (Merck), and counted.

Oligomerization assay

To perform a coimmunoprecipitation-based oligomerization assay, plasmids (0.5 μg) expressing HA-tagged wild-type and mutant hA3G were transfected along with phA3G-myc (0.5 μg) into 293T cells using FuGENE 6. After 48 h, the transfected cells were suspended in 500 μl of RIPA buffer (50 mM Tris-HCl, pH 7.4, 150 mM NaCl, 1% NP-40, 0.5% sodium deoxycholate, 0.1% SDS, complete protease inhibitor cocktail [Roche]). The resultant lysates were clarified by brief centrifugation, pre-cleared with 30 μl of Protein A-Agarose Fast Flow (GE Healthcare) for 1 h at 4°C, and then incubated with an anti-myc affinity gel (Sigma). After 1 h at 4°C, the immune complexes were extensively washed with RIPA buffer. Equal aliquots of the total and bound fractions were subjected to gel electrophoresis and transferred to a nitrocellulose membrane. The membranes were probed with an anti-HA mouse monoclonal antibody (Sigma) or an anti-β-actin mouse monoclonal antibody (AC-74, Sigma). The signal intensities of the immunoprecipitated hA3G protein on Western blots were quantified using the LAS-3000 imaging system (Fujifilm). For the RNase A treatment experiment, the immune complexes were separated into two aliquots. The wild-type sample was incubated with or without 25 U of RNase A (Sigma) at room temperature for 30 min. Samples were extensively washed and then resuspended in loading dye. The samples were assayed as described above.

Molecular modeling of the head-to-head dimer structure of the N-terminus of hA3G

Head-to-head dimer models of hA3G N-terminal domain were obtained by homology modelling using either the crystal structure of human APOBEC2 (hA2) at a resolution of 2.50 Å or the NMR structure of the C-terminal domain of hA3G (PDB code: 2NYT chain A [56] or 2JYW [57], respectively) as a template, as previously performed [34,58-60]. To minimize misalignments between the hA3G N-terminal domain as a target sequence and either hA2 or the C-terminal domain of hA3G as a template sequence, we used the multiple sequence alignment method with the sequences of hA3A (GenBank accession number: NM_145699), hA3C (GenBank accession number: NM_014508), and hA3F (GenBank accession number: NM_145298). Multiple sequence alignments were generated using 'MOE-Align' in Molecular Operating Environment (MOE) version 2010.10 (Chemical Computing Group Inc., Quebec, Canada). Three-dimensional (3-D) models of the hA3G N-terminal domain were constructed by the homology modeling technique using 'MOE-Homology' in MOE as previously described [61]. We obtained 25 intermediate models per homology modeling session in MOE, and we selected the 3-D models that were intermediate models with best scores according to the generalized Born/volume integral methodology [62]. The 3-D structure was thermodynamically optimized by energy minimization using MOE and an AMBER99 force field [63] combined with the generalized Born model of aqueous solvation implemented in MOE [64]. The physically unacceptable local structure of the optimized 3-D model was further refined based on the evaluation of the Ramachandran plot using MOE.

Results

hA3 family members differentially inhibit Alu retrotransposition

To determine if hA3 family members are able to inhibit *Alu* retrotransposition as well as L1 retrotransposition [37], we performed a neo^r-based retrotransposition assay [5]. In this assay system, we utilized a L1 ORF2 expression plasmid that is required for *Alu* retrotransposition [53], together with an *Alu* clone DNA carrying a reverse-oriented neo^r gene separated by a gamma-globin intron. After transfection of the cells with this construct, neo^r with *Alu* is transcribed, spliced, reverse-transcribed, and integrated. Then, the neo^r gene that is integrated with *Alu* is driven by the CMV promoter and expressed. After G418 selection following transfection, we were able to quantify the retrotransposition level by counting the number of G418^R colonies. hA3 protein expression in the cells were confirmed by immunoblotting using anti-HA antibodies (Figure 1A). Without the co-expression of an hA3 protein, *Alu* retrotransposition occurred at the level shown in the upper left panel of Figure 1B. In contrast, the co-expression of any of the hA3 proteins differentially inhibited *Alu* retrotransposition, and in particular, the expression of hA3A, hA3B, or hA3G strongly decreased the transposition level of *Alu* elements (Figure 1C). Thus, we conclude that hA3 proteins act to differentially suppress *Alu* retrotransposition. Importantly, in agreement with previous reports [34-36,39], we observed that hA3G has an inhibitory effect on *Alu* retrotransposition in the assay. It should be noted that these activities against *Alu* correlated exactly with the patterns previously observed for the inhibition of L1 [37].

The *N*-terminal 30 amino acids of hA3G determine the inhibitory effect on Alu retrotransposition

Because hA3G is the best characterized hA3 family member protein, we focused on this protein and attempted to determine the region responsible for its anti-retrotransposon activities. To identify the relevant region, we created a series of mutants with serial deletions from the N-terminus up to amino residue 150 (Figure 2A). Protein expression in the cells transfected with each plasmid was confirmed by immunoblotting using an anti-HA antibody (Figure 2B). hA3G mutants lacking the C-terminal domain were undetectable as previously reported [34,65] and therefore could not be used for further experiments. Immunofluorescence microscopy confirmed that hA3G deletion

Oligomerized hA3G inhibits retrotransposition

Figure 1

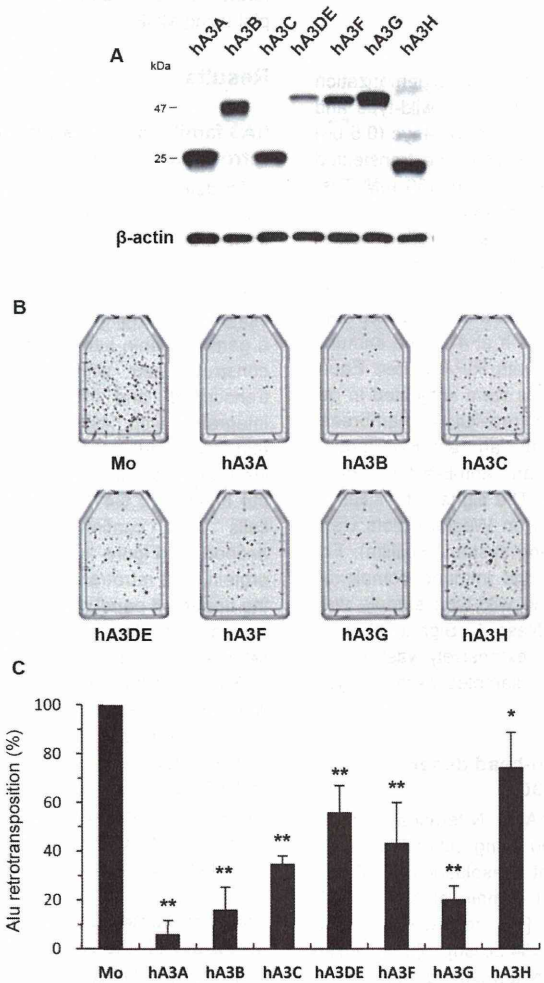

Figure 1. hA3 proteins inhibit Alu retrotransposition at differential levels. (**A**) Western blot analysis was performed by using extracts from 293T cells transfected with HA-tagged hA3 expression plasmids. Antibodies specific for HA were used. (**B**, **C**) HeLa cells were cotransfected with the *neo*^{r}-based *Alu* expression vector pYa5neotet and the L1 ORF2 expression plasmid pBudORF2opt, together with the respective hA3 expression plasmid. Seventy-two hours later, the cells were trypsinized, re-seeded into T25 or T75 flasks, and subjected to G418 (400 μg/ml) selection. At 14 days after selection, the resultant G418^R colonies fixed, stained with crystal violet (B), and counted to determine the level of *Alu* retrotransposition (C). The retrotransposition level in the absence of hA3 proteins was set to 100%. The data shown are the mean ± SD of triplicate experiments. Mo, mock. $^*P < 0.05$, $^{**}P < 0.005$, *t*-test.

doi: 10.1371/journal.pone.0084228.g001

mutant proteins other than NΔ150 were predominantly localized to the cytoplasm, as was the wild-type protein (Figure 2C). These deletions also abrogated the anti-HIV-1 activity of hA3G (Figure S1). We performed an *Alu* retrotransposition assay by transfecting HeLa cells with the *Alu* expression plasmid, the L1 expression plasmid, and a wild-type or mutant hA3G plasmid, and we observed that the deletion of 30 or more residues from the N-terminus of hA3G completely abrogated the inhibitory activity of hA3G on *Alu* retrotransposition (Figures 2D and 2E). We therefore conclude that the N-terminal 30 amino acids of hA3G are critical for the inhibition of *Alu* retrotransposition.

The inhibitory effect of hA3G on Alu retrotransposition is associated with its oligomerization and is independent of its deaminase activity

The anti-HIV-1 activity of hA3G is known to be dependent on two different activities, deamination and oligomerization, the former of which has been shown to be disrupted by the mutation of E259 located in the C-terminal cytidine deaminase (CD2) [65,66], and the latter of which has been reported to be abrogated by the mutation of C97 and C100 located in the N-terminal cytidine deaminase (CD1) [65]. Based on these past findings, we wished to determine which functions of hA3G are crucial for blocking the ability of *Alu* to retrotranspose. We created plasmids expressing hA3G defective in either oligomerization or deamination (C97/100A or E259Q, respectively; Figure 3A) and confirmed the expression of these proteins by immunoblotting using an anti-HA antibody (Figure 3B). Interestingly, the *Alu* retrotransposition assay revealed that the C97/100A oligomerization mutant of hA3G had no inhibitory activity against *Alu* retrotransposition, whereas the E259Q deamination mutant retained wild-type activity (Figure 3C). These observations confirmed the previous results [34,35], showing that the inhibition of *Alu* retrotransposition by hA3G is not due to the ability of hA3G to deaminate this retrotransposon but is due to its ability to form an oligomer.

The *N*-terminal 30 amino acids of hA3G are required for the oligomerization of this protein

Because hA3G's inhibitory activity against *Alu* retrotransposition was abolished in the mutants carrying an N-terminal deletion of 30 or more residues (Figure 2) and in the oligomerization mutant harboring mutations at amino acid positions 97 and 100 (Figure 3), we reasoned that the N-terminal 30 amino acids of hA3G might be critical for its ability to form oligomers. To test this hypothesis, we performed an oligomerization assay by coexpressing wild-type hA3G tagged with Myc and the mutant hA3Gs tagged with HA. The cell lysates were then immunoprecipitated with an anti-HA antibody and immunoblotted with an anti-Myc antibody. As shown in Figure 4, the E259Q deamination mutant of myc-tagged hA3G was efficiently coimmunoprecipitated with the HA-tagged wild-type protein. In contrast, the N-terminal serial deletion mutants lacking 30 or more residues completely lost the ability to oligomerize, as did the C97/100A mutant. When the immunoprecipitated samples were treated with RNase A, the oligomerization efficiency of hA3G was moderately decreased (Figure S2), consistent with the previous reports that cellular RNA might contribute to the stabilization of hA3G's oligomer [34]. Thus, the 30 amino acids at the N-terminus of hA3G are responsible for its oligomerization.

The *N*-terminal 30 amino acids of hA3G are the structural key for its oligomerization

To fully understand the mechanism by which N-terminal 30 amino acids of hA3G regulate oligomerization, we analyzed the effect of the deletion of the N-terminal 30 amino acids on the predicted 3-D structure of the hA3G dimer that was reported to be the major form of hA3G oligomer [34,59]. Thermodynamically stable N-terminal structures of wild-type hA3G and its N-terminal 30-amino-acid deletion mutant were constructed by homology modeling using the hA2 crystal structure as a template. As shown in Figures 5A and B, when the structures of the wild-type and deletion mutant hA3G proteins were compared, it was obvious that the N-terminal 30 amino acids (shown in cyan in Figure 5A) were present along the contact surface of the hA3G dimer, and therefore, the deletion of this region could abolish the interaction interface between the two hA3G molecules. We thus conclude that the N-terminal 30 amino acid residues of hA3G are located at the dimer interface and are critical for oligomerization.

Residues 24–28 contribute to the ability of hA3G to homooligomerize and inhibit Alu retrotransposition

Next, we analyzed the interaction interface of the hA3G dimer by structural modeling based not only on the hA2 crystal structure but also on the C-terminal hA3G (hA3G-C) NMR structure in parallel. Both structural modeling of wild-type hA3G revealed that, among the N-terminal 30 amino acids, a cluster of dimer interface residues (R24, P25, I26, L27, and S28) located in the N-terminal core structure α1-loop-β1 of hA3G interact with the counterpart residues of another monomer (Figures 6A and 6B). Importantly, this interface corresponds structurally (but not genetically) to a part of the potential oligomerization interfaces of the hA3G C-terminal domain, as described by Shandilya et al. [67]. At this putative interaction surface (Figures 6A and 6B), R24 likely interacts with D130 of another monomer through hydrogen bonds and electrostatic interactions, whereas the isoleucine/leucine residues at positions 26/27 can form a hydrophobic interaction with the counterpart residues of another monomer. hA2-based modeling shows that the serine residue at position 28 forms another hydrogen bond with the counterpart residues of another monomer (Figure 6A), although the same residue in hA3G-C-based modeling appears to be slightly separated from the counterpart residue of another monomer (Figure 6B). Additionally, the structural stability would be enhanced by a proline residue at position 25 in the loop. Thus, we speculated that the mutation of these residues might abolish the oligomerization of hA3G. To test this hypothesis, we first addressed whether structural modeling would be able to distinguish oligomerization-deficient and oligomerization-intact hA3Gs by analyzing the model of an hA3G mutant (hA3G-4G(124–127)), in which we introduced the small amino acid glycine in place of the aromatic amino acid residues

Figure 2

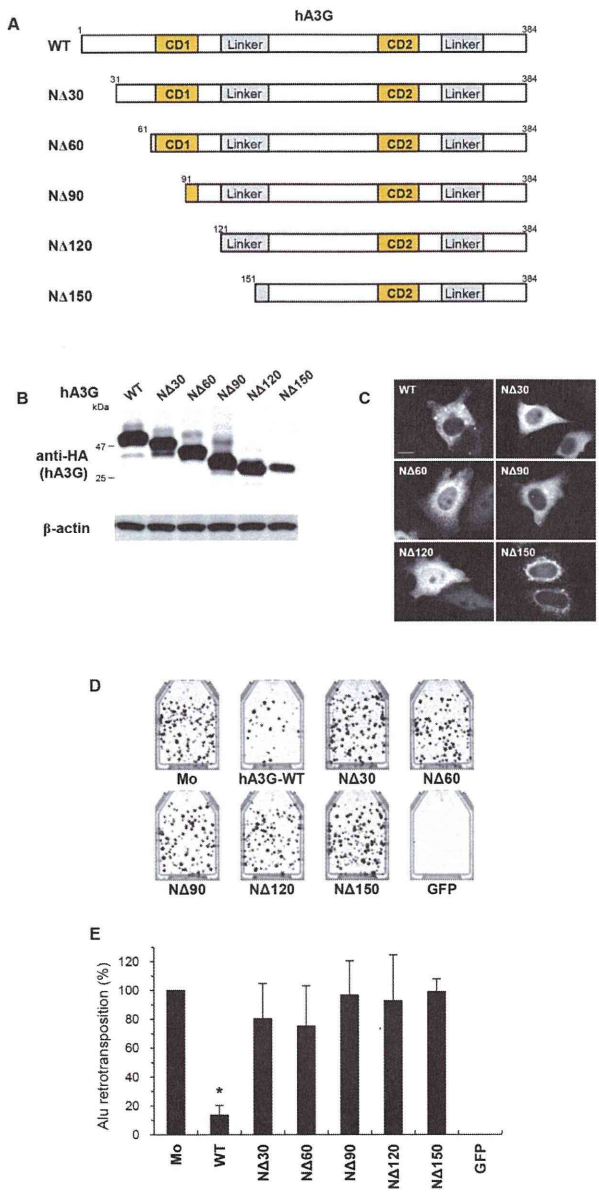

Figure 2. The N-terminal 30 amino acids regulate the anti-Alu activity of hA3G. (**A**) Schematic depiction of a series of N-terminal deletion mutants of hA3G. CD1, N-terminal cytidine deaminase; CD2, C-terminal cytidine deaminase. (**B**) Western blot analysis was performed using extracts from 293T cells transfected with plasmids expressing HA-tagged hA3G mutant proteins. Monoclonal antibodies specific for HA (upper) or β-actin (lower) were used. (**C**) Representative images of HeLa cells transfected with the indicated plasmids are shown. hA3G wild-type (WT), NΔ30, NΔ60, NΔ90, and NΔ120 mutant proteins were predominantly localized to the cytoplasm, whereas NΔ150 mutant protein localized to the perinuclear region. Scale bar: 20 μm. (**D**, **E**) An *Alu* retrotransposition assay was performed as described in Figure 1. Crystal violet-stained G418^R colonies were counted to determine the level of *Alu* retrotransposition. The data shown are the mean ± SD of triplicate experiments. Mo, mock; WT, wild-type hA3G; GFP, GFP only. *$P < 0.005$, *t*-test.

doi: 10.1371/journal.pone.0084228.g002